ACS NANO
Cite This: ACS Nano 2017, 11, 9836-9845
www.acsnano.org

ARTICLE

# High-Resolution Graphene Films for Electrochemical Sensing *via* Inkjet Maskless Lithography

John A. Hondred,[†] Loreen R. Stromberg,[†] Curtis L. Mosher,[‡] and Jonathan C. Claussen*[,†]

[†]Department of Mechanical Engineering and [‡]Department of Genetics, Development and Cell Biology, Iowa State University, Ames, Iowa 50011, United States

Supporting Information

**ABSTRACT:** Solution-phase printing of nanomaterial-based graphene inks are rapidly gaining interest for fabrication of flexible electronics. However, scalable manufacturing techniques for high-resolution printed graphene circuits are still lacking. Here, we report a patterning technique [*i.e.*, inkjet maskless lithography (IML)] to form high-resolution, flexible, graphene films (line widths down to 20 $\mu$m) that significantly exceed the current inkjet printing resolution of graphene (line widths ~60 $\mu$m). IML uses an inkjet printed polymer lacquer as a sacrificial pattern, viscous spin-coated graphene, and a subsequent graphene lift-off to pattern films without the need for prefabricated stencils, templates, or cleanroom technology (*e.g.*, photolithography). Laser annealing is employed to increase conductivity on thermally sensitive, flexible substrates [polyethylene terephthalate (PET)]. Laser annealing and subsequent platinum nanoparticle deposition substantially increases the electroactive nature of graphene as illustrated by electrochemical hydrogen peroxide ($H_2O_2$) sensing [rapid response (5 s), broad linear sensing range (0.1−550 $\mu$m), high sensitivity (0.21 $\mu$M/$\mu$A), and low detection limit (0.21 $\mu$M)]. Moreover, high-resolution, complex graphene circuits [*i.e.*, interdigitated electrodes (IDE) with varying finger width and spacing] were created with IML and characterized *via* potassium chloride (KCl) electrochemical impedance spectroscopy (EIS). Results indicated that sensitivity directly correlates to electrode feature size as the IDE with the smallest finger width and spacing (50 and 50 $\mu$m) displayed the largest response to changes in KCl concentration (~21 k$\Omega$). These results indicate that the developed IML patterning technique is well-suited for rapid, solution-phase graphene film prototyping on flexible substrates for numerous applications including electrochemical sensing.

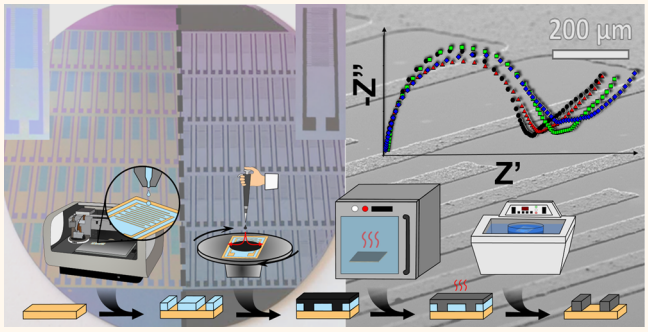


**KEYWORDS:** *graphene, inkjet printing, flexible electronics, scalable nanomanufacturing, electrochemical sensing*



Solution-phase printing of nanomaterial-based conductive inks has helped facilitate the scalable manufacturing of flexible electronics[1−3] in a low-cost, high-throughput fashion.[4−6] These printing protocols have expedited the advent of new technologies for diverse applications including those associated with energy storage,[7] flexible electronic displays,[8] smart packaging,[9] and diagnostic sensors.[10] Graphene-based inks have shown great promise in enabling these applications due to inherently advantageous material properties (*e.g.*, high mechanical flexibility, electrical and thermal conductivity, chemical and environmental robustness, and biocompatibility).[11−14,31,32] Numerous graphene printing techniques, such as screen, gravure, and inkjet printing, have been developed to coat graphene flakes onto flexible and nonflexible surfaces.[15,16] However, these techniques are often limited by low line resolution patterning (>50 $\mu$m).

Recently, a variety of manufacturing tools have been developed to increase the line resolution of printed graphene films such as gravure templates and silicon stencils with line resolution of printed graphene films of 30 and 5 $\mu$m, respectively.[17,18] However, these techniques require the use of cleanroom technology (*i.e.*, photolithography) to fabricate a stencil or gravure template for each new pattern design. Photolithography requires multiple fabrication steps including photoresist application, development, and removal as well as UV exposure through a chrome/glass mask. This makes photolithography costly, time-consuming,[19] and inadequate for rapid prototyping of electrical circuits.[17,18,20] Other groups

Received: May 21, 2017
Accepted: September 20, 2017
Published: September 20, 2017




DOI: 10.1021/acsnano.7b03554
ACS Nano 2017, 11, 9836−9845

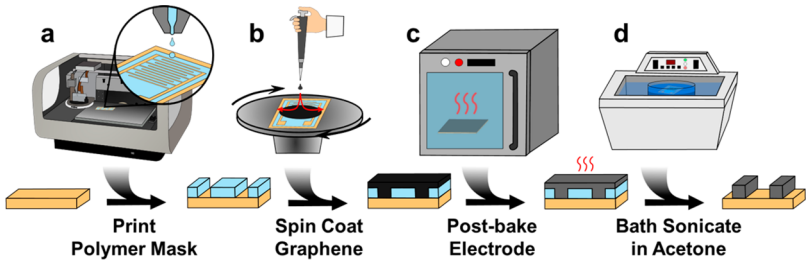


**Figure 1. Schematic depicting the four-step manufacturing process for IML graphene patterning. (a) Sacrificial polymer layer is inkjet printed onto the substrate as the negative design pattern. (b) Highly concentrated graphene ink is spin-coated evenly over the entire surface. (c) Postbake process increases the adhesion of the graphene to the substrate. (d) Sacrificial layer is removed, and graphene lift-off occurs with a sonicated acetone bath to produce the final graphene pattern.**

have developed electrostatic spray deposition (ESD) to create interdigitated electrodes (IDEs) with finger width and spacing of 100 and 50 $\mu$m, respectively.[21] However, similar to previous techniques, this solution-phase graphene technique requires the need for photolithography patterning.

Inkjet printing is a scalable, cost-effective, and versatile technique for depositing highly intricate patterns on multiple substrates. This process does not require fixed geometry masks/stencils or the need to use photolithography patterning.[19] Moreover, inkjet printing has several advantages including large surface area coverage, scalability for mass production, capability of printing on flexible substrates, and rapid prototyping through the use of computer-aided design (CAD) software.[22,23] The major limitation of inkjet printing is the narrow value range that ink fluid properties (*e.g.*, viscosity, surface tension, and density) must fall within for consistent droplet formation and pattern printing. For example, a typical inkjet printable ink must have a viscosity between 2 and 20 cP, surface tension between 30 and 40 mN/m, particle size less than 1% of the nozzle diameter, and a specific gravity of 1−1.5.[24] With such stringent requirements, suspending large particle inks that can be printed with high resolution, without clogging nozzles, splattering, or inconsistencies in ink deposition, is technically challenging.

Herein, we demonstrate a photolithography-free, high-resolution solution-phase graphene patterning technique, coined inkjet maskless lithography (IML). The IML technique can be used to pattern graphene films onto virtually any 2D planar substrate from rigid, temperature-resistant silicon to flexible, inflammable polymers. The method is accomplished by inkjet printing a polymer pattern, spin-coating a more viscous/dense solution-phase graphene layer, and removing the polymer pattern *via* a solvent-based lift-off process to create the patterned graphene film. This inkjet printed patterning technique circumvents the need for developing templates and is conducive to scalable roll-to-roll manufacturing onto flexible substrates.[22,23] Moreover, IML can be used to create graphene line resolutions of 20 $\mu$m—therefore superseding the typical resolution limitations of inkjet printing which is typically line resolution of 60 $\mu$m or greater.[25] Some researchers have demonstrated inkjet printing polymers as a protective mask,[26−28] whereas others have inkjet printed polymer layers for a sacrificial lift-off process as displayed in coffee-ring lithography[29] and polymer microsieve pores.[30] However, full patterning of high-resolution (<25 $\mu$m) graphene circuits has not been previously addressed. Furthermore, we demonstrate the electrochemical utility of the developed graphene films by creating a hydrogen peroxide ($H_2O_2$) sensor printed on flexible Kemafoil polymer substrate (heat-treated PET). The patterned graphene was laser-annealed and electrodeposited with platinum nanoparticles to increase electrode sensitivity. Finally, graphene IDE arrays with varying finger width and spacing (50 and 50 $\mu$m; 75 and 150 $\mu$m; 150 and 200 $\mu$m, respectively) were manufactured and subsequently characterized with electrochemical impedance spectroscopy (EIS) to demonstrate the ability to create high-resolution graphene circuits using IML.

## RESULTS AND DISCUSSION

**Graphene Patterning *via* Inkjet Maskless Lithography (IML).** *Overview of the IML Process Steps.* The IML manufacturing protocol developed herein uses a four-step process to make conductive graphene patterns (Figure 1). First, the negative of the desired graphene pattern is inkjet printed (designed with CAD software and uploaded to the printer) onto the substrate with a sacrificial polymer (Figure 1a and Experimental Methods). Next, graphene ink, made with a higher concentration of graphene than inkjet printable inks (*e.g.*, 15 mg/mL *vs* ∼3.5 mg/mL),[31−33] is spin-coated over the pattern (Figure 1b and Experimental Methods). Graphene adhesion is increased, and ink solvents are removed *via* heating (postbake) in an oven (Figure 1c and Experimental Methods). Finally, the polymer pattern is removed and graphene lift-off occurs by exposing the substrate to a sonicated acetone bath (10 s) and/or direct acetone impingement with a wash bottle (Figure 1d).

*Sacrificial Polymer Ink Formulation and Printing.* The physical properties of the sacrificial polymer ink are critically important to create a high-resolution negative pattern. The fluid dynamic properties of the ink (*viz.*, viscosity, surface tension, and density) strongly influence the inkjet printed line/pattern resolution. Primarily, two different nondimensional properties [Reynolds number (eq 1) and Weber number (eq 2)], which are related to the inertial forces of viscosity and surface tension, govern the printability of an ink.

$$\mathrm{Re} = \frac{v\rho a}{\eta} \tag{1}$$

$$\mathrm{We} = \frac{v^2\rho a}{\gamma} \tag{2}$$

$$Z = \frac{1}{\mathrm{Oh}} = \frac{\mathrm{Re}}{\sqrt{\mathrm{We}}} = \frac{(\gamma\rho a)^{1/2}}{n} \quad \text{where } 10 > Z = \frac{1}{\mathrm{Oh}} > 1 \tag{3}$$

$$K_c = \mathrm{We}^{0.5} \times \mathrm{Re}^{0.25} \quad \text{where } K_c < 100 \tag{4}$$

where $v$ is the impact velocity, $\rho$ is the ink density, $a$ is the drop diameter before impact, $\eta$ is the viscosity of the ink, and $\gamma$ is the



DOI: 10.1021/acsnano.7b03554
ACS Nano 2017, 11, 9836−9845

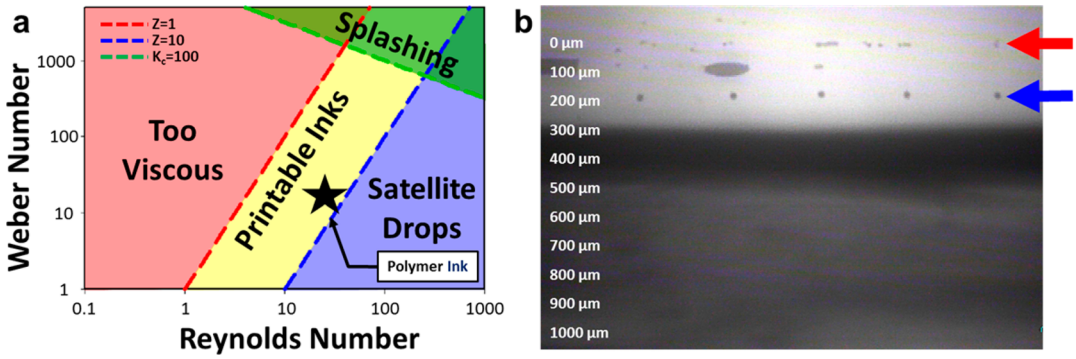


**Figure 2. Polymer lacquer fluid properties. (a) Graphical representation of optimized inkjet printing parameters plotted *versus* the nondimensional Reynolds and Weber numbers. Star indicates where the developed printable polymer ink falls within these parameters. (b) Optical image of the polymer ink (diameter ~ 10 $\mu$m) without any satellite droplets. The red arrow points to the 1 pL nozzle tips, and the blue arrow indicates droplets acquired immediately after expulsion from the inkjet printer nozzle.**

surface tension. The *Z*-value (inverse of the Ohnesorge number, Oh), which describes the overall jettability of an ink (eq 3), combines Reynolds and Weber numbers and does not depend on the velocity of the jetted ink. For proper jetting to occur, Reis and Derby *et al.* estimated the *Z*-value should be between 1 and 10 and the drop impact (eq 4) be below 100.[34] At low *Z*-values (<1) the viscosity of the ink is too large for proper ejection of the droplet, whereas at high *Z*-values (>10), unwanted satellite droplets form. When the drop impact approaches 100, splashing upon impact is predicted, which decreases printing resolution. In this work, the sacrificial polymer ink was developed with the solvent cyclohexanone and terpineol, similar to previously reported jettable inks.[23,31] These solvents were subsequently mixed with an acrylic lacquer at a ratio of 8:1:1 (Experimental Methods). This ink displayed a Reynolds number of 30.8, Weber number of 26.9, and a *Z*-value of 5.9 when printed at 40 °C, which falls within the region of printable inks (Figure 2a).[34] Hence, the developed polymer ink printed without satellite droplets did not splash when deposited onto the substrate and formed consistently stable drops upon expulsion from the piezoelectric nozzle of the inkjet printer (Figure 2b, blue arrows; Supplemental Movie 1 and Experimental Methods). The polymer printing process was adjusted (nozzle temperature set to 40 °C, 20 $\mu$m drop spacing) to develop well-defined printed lines (50−75 $\mu$m width), straight edges, and spacing between polymer layers below 25 $\mu$m (Experimental Methods). Upon impact, the inkjet printed polymer droplets coalesced into a film (Figure S1).

*Graphene Spin-Coating and Postbake.* Another important aspect for obtaining high-resolution graphene films is properly controlling the temperature and time of the graphene postbake. Recall that after the negative pattern is inkjet printed onto a substrate, a viscous graphene ink is spun over the polymer patterned surface (Figure 1 and Experimental Methods). A temperature- and time-controlled baking process is subsequently conducted in a convection oven to remove ink solvents and simultaneously improve the physical bond between the substrate and the graphene (Figure 3).[33] At low baking temperatures and/or short baking times, the graphene did not adhere tightly to the substrate and was completely removed upon acetone lift-off of the sacrificial polymer (Figure 3, top left). At higher baking temperatures or longer baking times, the polymer irreversibly hardened on the substrate, which inhibited acetone removal of the underlying sacrificial polymer (Figure 3, bottom right). However, a postbake temperature and time of

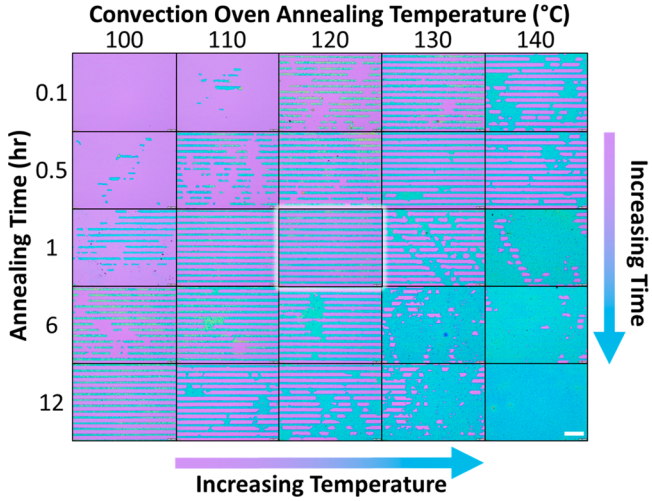


**Figure 3. A 5 × 5 panel of optical images illustrating the efficiency of the graphene lift-off method according to the temperature and time of the graphene postbake. Top left: Spin-coated graphene and sacrificial polymer are completely removed, exposing the bare Si/$SiO_2$ wafer (purple). Bottom right: Spin-coated graphene (green) completely covers the surface of the wafer as the underlying polymer sacrificial layer is not removed. Center: Highlighted center image shows high-resolution graphene lines with efficient graphene lift-off process. Scale bar equals 250 $\mu$m.**

120 °C for 1 h sufficiently adhered the graphene to the substrate while preventing overhardening of the sacrificial polymer so that it could be removed by acetone; this postbake time and temperature permitted the formation of well-defined graphene lines (25 $\mu$m width and 50 $\mu$m spacing) (Figure 3, center highlighted image). Note that a similar well defined pattern was formed after a post bake of 100 °C for 12 hours — of course such a long post bake is less than desirable and therefore this temperature and time for the postbake were not chosen.

*Graphene Annealing.* The electrical conductivity of the graphene films was increased by laser or thermal annealing processes similar to our previous protocols, where surfactants, solvents, and nonconductive binders (*e.g.*, ethyl cellulose) are burned off at lower temperatures (<300 °C) or lower laser energy densities (<50 mJ/cm$^2$) and morphological changes (*e.g.*, graphene flake fusion, superficial 3D nanostructuring, or semivertical graphene petal formation) occur at higher



DOI: 10.1021/acsnano.7b03554
*ACS Nano* 2017, 11, 9836−9845

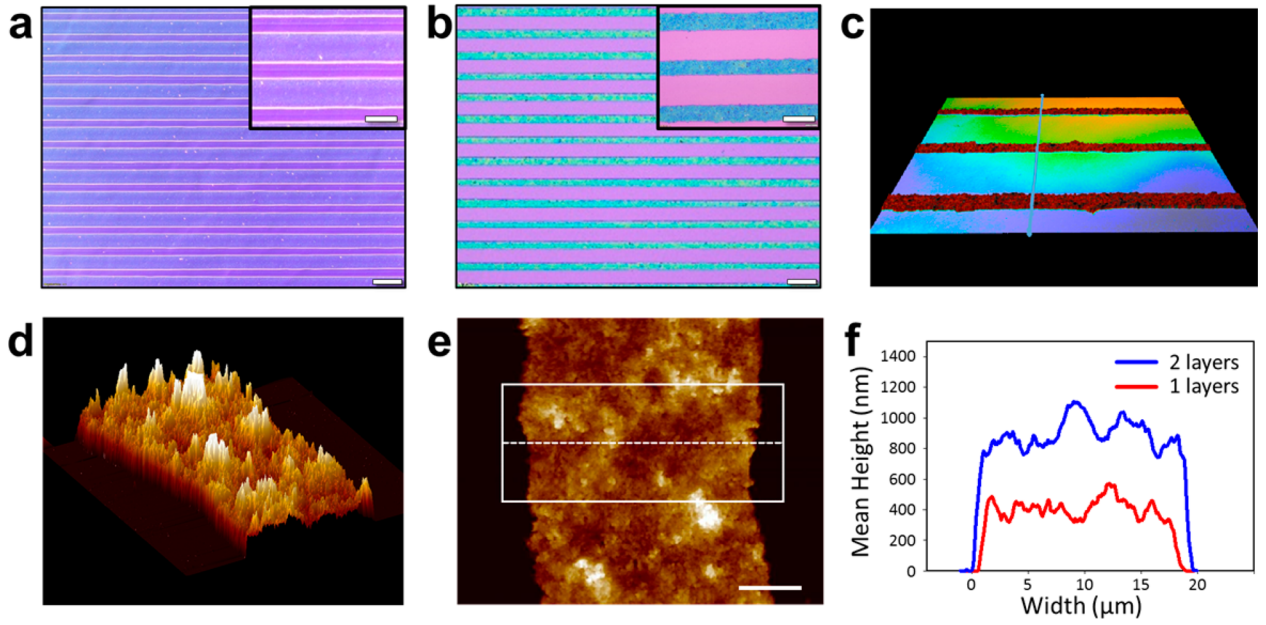


Figure 4. Line resolution of graphene patterned with the IML method $Si/SiO_2$ wafer. (a) Optical microscopy images of inkjet printed polymer sacrificial layer (scale bar 100 $\mu$m). Top right corner: Magnified inset shows 50 $\mu$m polymer lines with 20 $\mu$M spaces (scale bar 50 $\mu$m). (b) Graphene pattern after IML (scale bar 100 $\mu$m). Top right corner: Magnified inset showing 20 $\mu$m graphene lines (scale bar 50 $\mu$m). Printed graphene lines analyzed with (c) confocal microscopy, (d) cross-sectional 3D AFM imaging, and (e) top-view 2D AFM imaging. The dotted white line in (e) depicts the average cross section used to determine the graphene height profiles presented in (f). Averaged cross section height (f) of 1 (red) and 2 (blue) spin-coated layers of graphene using IML.

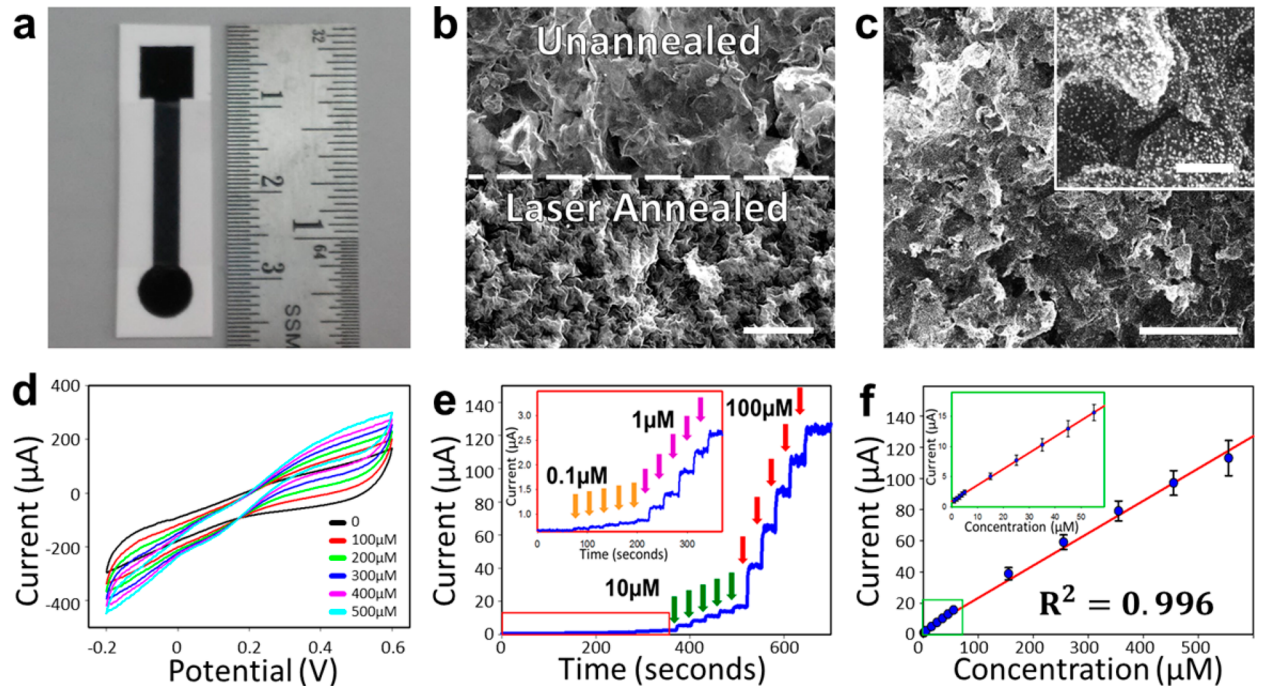


Figure 5. Electrochemical $H_2O_2$ sensing characterization with the IML graphene electrode on heat treated PET. (a) Graphene electrode fabricated with IML, laser-annealed, and electroplated with platinum nanoparticles to form a $H_2O_2$ sensor. (b) Scanning electron micrograph (SEM) of IML graphene electrode before (top) and after (bottom) laser annealing (scale bar 5 $\mu$m). (c) SEM of electrodeposited platinum nanoparticles onto graphene electrode (scale bar 5 $\mu$m). Top right corner: Magnification of typical platinum nanoparticles on graphene (scale bar 500 nm). (d) Cyclic voltammetry of $H_2O_2$ sensor in 1× PBS (black) with 100 $\mu$M $H_2O_2$ additions. (e) Amperometric $H_2O_2$ sensing showing current response for concentration step increases of 0.1 $\mu$m (orange arrows), 1 $\mu$m (purple arrows), 10 $\mu$m (green arrows), and 100 $\mu$M (red arrows) additions. Inset shows magnified view of 0.1 and 1 $\mu$M additions. (f) Concentration *versus* current graph illustrating the linear sensitivity of the $H_2O_2$ sensor. Inset shows magnified view of current response for 0.1, 1, and 10 $\mu$M concentration additions.

temperatures (>800 °C) or higher energy densities (>70 mJ/cm$^2$).[14,31−33] The initial resistance of the IML patterned graphene before annealing was 135 ± 15 kΩ ($n$ = 5) across a rectangular area of 25 mm × 3 mm. After thermal annealing at



DOI: 10.1021/acsnano.7b03554
ACS Nano 2017, 11, 9836−9845

1000 °C for 60 min, the resistance of the sample (patterned on a $Si/SiO_2$ wafer) was reduced to 3.5 ± 0.25 kΩ ($n$ = 5) (Figure S2). It is important to note that this annealing process was conducted in an inert ambient atmosphere, such as nitrogen, to ensure that the graphene did not oxidize at higher temperatures (>350 °C)—an effect that can subsequently hinder the electrical conductivity of the graphene.[23] Alternatively, laser annealing was used to anneal the IML patterned graphene on temperature-sensitive substrates (*e.g.*, Kemafoil, PET, polyimide) using a 1000 mW benchtop laser engraver. This laser annealing process (scan rate of 50 ms) reduced the graphene resistance to 329 ± 18 Ω ($n$ = 5) (Figure S2), which corresponds to a sheet resistance of ∼90 Ω/sq and electrical conductivity of ∼26 000 S/m.

Initially, the patterned graphene using the IML method is free of any oxygen functional groups. X-ray photoelectron spectroscopy (XPS) reveals distinct C−C bonds around 284 eV, which is a combination of $sp^2$ (284 eV) and $sp^3$ (284.8 eV) bonding structure, with no noticeable oxygen bonded to the graphene surface (Figure S3a). Upon laser annealing in an oxygen atmosphere, an additional shoulder peak appears that represents oxygen groups (C−O−C at ∼286.5 eV and C═O at ∼288.5 eV) on the surface of the graphene (Figure S3b). As graphene oxide is relatively not conductive, and the graphene patterned using IML is conductive, the oxygen groups are most likely localized to the surface of the graphene where the heat/energy of the laser facilitates ambient oxygen groups binding to superficial graphene flakes.

*Printing Resolution.* The printed graphene lines were characterized with both confocal and atomic force microscopy (AFM) (Figure 4). Results indicate that removal of the sacrificial layer (Figure 4a) leaves a conductive graphene pattern with high resolution down to 20 μm (Figure 4b), which is smaller than that of conventional inkjet printing techniques (∼50−100 μm).[23] Additionally, the IML process results in graphene lines with defined edges and relatively consistent height as opposed to inkjet printing which produces dome-like-shaped cross sections.[33] Confocal microscopy revealed IML graphene printed lines with 20 μm widths and 0.6 μm heights (Figure 4c), along with sharp edges and consistent spacing (Figure S4). AFM was subsequently used (Figure 4d) to analyze surface morphology, which displayed a relatively even graphene deposition, but with high surface area due to randomly oriented superficial graphene flakes. AFM also revealed a 0.4 μm steep step at the edge of the patterned graphene with relatively smooth morphology across the surface of a 20 μm printed graphene line (Figure 4e,f). The difference between AFM and confocal microscopy height measurements is most likely due to different test locations of the spin-coated graphene as spin-coating deposits material more heavily in the center and becomes thinner as distance from the axis of rotation increases. Spin-coating a second layer of graphene ink resulted in a doubling of the film thickness to 0.8 μm (see AFM measurements in Figure 4f; note that each height profile was acquired at the same location on the sample).

**Electrochemical $H_2O_2$ Sensing with Graphene Films.** The electrochemical sensing capability of the patterned graphene using the IML method was first characterized *via* $H_2O_2$ sensing. A graphene electrode (25 mm × 3 mm) was fabricated using IML and laser annealing (Figure 5a). We have shown previously[31] that laser annealing fuses/welds together graphene boundary layers and significantly increases the printed graphene surface area by nano/microstructuring the orientation of superficial graphene flakes (Figure 5b). Laser annealing was used to increase the surface area and superficial defects which are well-suited for electrochemical, heterogeneous charge transport, and metallic nanoparticle deposition.[35,36] Platinum nanoclusters (∼25−50 nm diameter spheres) were subsequently electrodeposited onto the surface of the electrode, according to our previous protocols (Figure 5c and Experimental Methods),[36,37] as it is an efficient non-enzymatic catalyst for peroxide sensing. The laser-annealed, high surface area graphene not only acts as a conductive transduction material but also provides an effective scaffold structure for the platinum nanoclusters. We have shown in similar studies that this graphene/platinum hybrid dramatically improves $H_2O_2$ sensing over platinum alone.[36,38,39]

To electrochemically characterize the platinum−graphene sensors, cyclic voltammetry and amperometry were conducted with a standard three-electrode setup (Figure 5d−f). Cyclic voltammograms acquired with increasing concentrations of $H_2O_2$ (100 μM final concentration additions, from 0 to 500 μM) revealed that peak oxidation occurred at a voltage of approximately +0.4 V (Figure 5d). Subsequent amperometric measurements (Figure 5e,f) were conducted at a working potential of +0.4 V for increasing concentrations of $H_2O_2$ (*i.e.*, 5 increments of 0.1, 1, 10, and 100 μM). These amperometric results show a wide linear $H_2O_2$ sensing range (0.1 to 550 μM, $R^2$ = 0.996), high sensitivity (0.21 μM/μA), low detection limit [0.21 ± 0.16 μM (3σ)], and a fast response time (∼5 s). The $H_2O_2$ sensor compared favorably to those achieved by similar carbon/metal hybrids electrodes while eliminating the need for multiple processing steps (*e.g.*, electrode polishing, drying under infrared lamps, multiple electrodeposition steps, and sonication cleaning) (Table 1).

**Graphene Interdigitated Electrode Film Fabrication and Characterization.** To demonstrate the patterning and resolution capabilities of IML, complex graphene patterns and a high-resolution IML logo were developed and characterized

**Table 1. Performance Comparison Table of Electrochemical $H_2O_2$ Sensors Comprising Carbon Nanomaterial/Metal Nanoparticle Hybrids**[a]

| electrode | operating potential (V) | linear range (μM) | detection limit (μM) | ref |
|---|---|---|---|---|
| PtAu NC graphene GCE | +0.1 | 0.82−8.73 | 0.008 | 40 |
| PNEGHNS | 0 | 1−500 | 0.008 | 41 |
| OMCs/GE | +0.35 | 0.1−500 | 0.032 | 42 |
| GNPs/GN-CS/GCE | −0.4 | 5−35000 | 1.6 | 43 |
| CQDs/octahedral $Cu_2O$ | −0.2 | 5−5300 | 2.38 | 39 |
| CNF-PtNP/GCE | −0.34 | 10−9380 | 1.9 | 44 |
| IML Pt-graphene | +0.4 | 0.1−550 | 0.21 | this work |

[a]PtAu NC graphene GCE: platinum−gold nanoclusters on glassy carbon electrode. PNEGHNS: platinum nanoparticle ensembled-on-graphene hybrid nanosheet. OMCs/GE: ordered mesoporous carbons modified glassy carbon electrode. GNPs/GN-CS/GCE: gold nanoparticle graphene chitosan modified glassy carbon electrode. CQDs/octahedral $Cu_2O$: carbon quantum dots octahedral cuprous oxide nanocomposites. CNF-PTNP/GCE: nanoporous carbon nanofibers decorated with platinum nanoparticles on glassy carbon electrode. IML Pt-graphene: inkjet maskless lithography electrodeposited platinum on graphene.



DOI: 10.1021/acsnano.7b03554
ACS Nano 2017, 11, 9836−9845

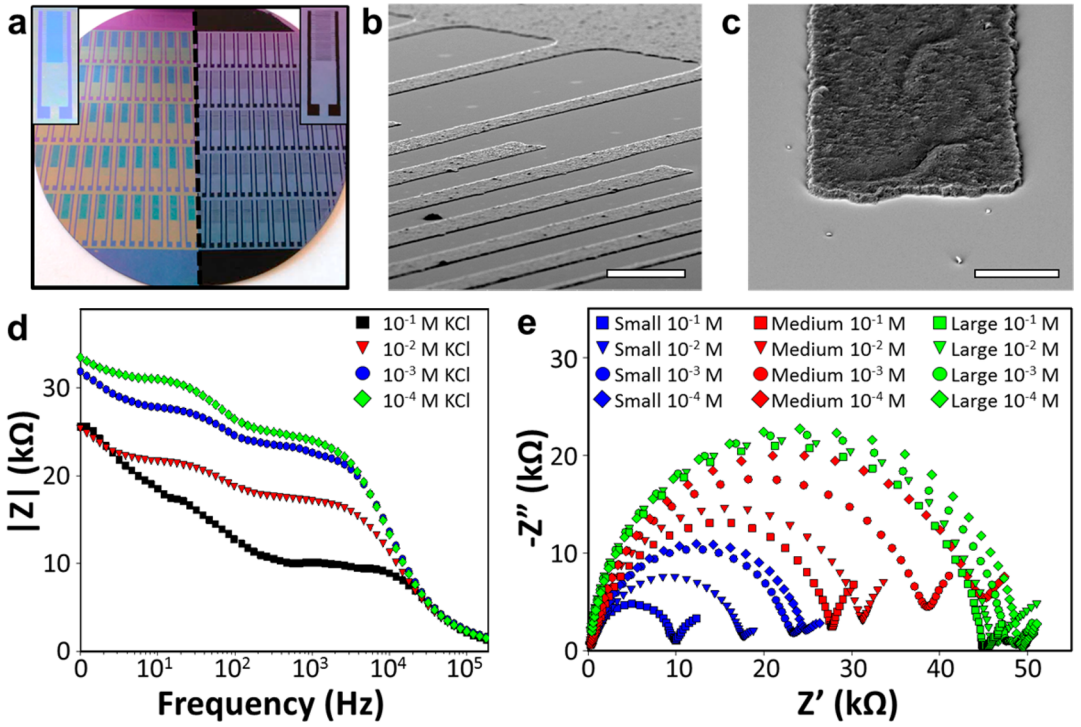


**Figure 6. IML graphene design and IDE characterization. (a) Array of IDEs showing the negative IDE inkjet printed pattern using a sacrificial polymer layer (left) and the resultant graphene IDE pattern after IML on a silicon wafer (right). Top corner images show magnified view of IDE patterns. (b) High-resolution tilted-view SEM micrograph of resultant graphene IML IDE (scale bar 100 $\mu$m). (c) SEM displaying edge of graphene pattern (scale bar 20 $\mu$m). (d) Diagram of total impedance *versus* frequency for various concentrations of KCl (Bode plot). (e) Nyquist impedance plots for three different size IDEs with four distinct concentrations of KCl.**

(see Supplemental Movie 2). It should be noted here that such IML patterning is not limited to graphene inks, but can also be conducted with other inks such as those derived from metallic nanoparticles (*e.g.*, silver nanoparticles) (see Figure S5). An IDE array, a pattern consisting of two electrodes in alternating parallel bands with "comb-like features" that experiences large collection efficiencies,[45] increased signal-to-noise ratios,[46] fast response times,[47] as well as no need for a separate reference electrode during electrochemical sensing,[48] was next created with IML to test the electrochemical reactivity of such high-resolution graphene patterning. The IML graphene IDE was fabricated with finger widths of 50 $\mu$m and interfinger spacing of 75 $\mu$m on a silicon wafer (Figure 6b and Figure S6). Scanning electron micrograph (SEM) images of the graphene IDEs displayed well-defined graphene patterns with sharp edges, straight lines, and consistent widths (Figure 6b,c and Figure S7). A high-resolution SEM corroborated the previous AFM measurements by displaying a sharp step height on the edge of the graphene pattern and a flat textured surface with high surface area due to the randomly oriented graphene flakes.

The graphene IDEs were electrochemically characterized by alternating current nonfaradaic EIS in varying concentrations ($10^{-1}$, $10^{-2}$, $10^{-3}$, and $10^{-4}$ M) of potassium chloride (KCl). The direct relationship of impedance with frequency was analyzed *via* the Bode plot (Figure 6d). At lower frequencies (below 10 Hz), the impedance is related to the double layer capacitance, whereas at higher frequency (above 10 000 Hz), the dielectric region governs the impedance.[49] The region between the double layer and the dielectric region is due to the solution resistance in which changes in the concentration of ions and their mobility were analyzed. Subsequently, increasing the KCl concentration resulted in increased impedance in both the double layer and solution resistance regions.

Next, three distinctly sized graphene IDEs with two 10-finger combs of varying finger width and spacing (50 and 50 $\mu$m; 75 and 150 $\mu$m; 150 and 200 $\mu$m; finger width and spacing, respectively) were created with IML. Resulting electrodes were characterized by EIS, and the real *versus* imaginary impedance was plotted (Figure 6e). All graphene IDEs displayed typical Nyquist impedance characteristics: semicircle shapes with straight tails (45° straight line after semicircle) where the semicircular region (high frequency) is kinetically controlled and the tail region (low frequency) characterizes the mass-transfer-controlled section (diffusion-limited process).[50] The double layer capacitance of the graphene IDE (50 $\mu$m finger width and 50 $\mu$m finger spacing) was calculated to be ~5 nF in 0.1 M KCl, which is comparable to IDEs comprising palladium,[51] gold,[52,53] and carbon nanotubes[54] (Experimental Methods). As the concentration of KCl increased, the equivalent film resistance increased, making the system kinetically slower (wider semicircle) for each of the different feature sized graphene IDEs. As expected, the graphene IDE with larger feature sizes displayed larger film resistance ($R_{ct}$, diameter of semicircle). Additionally, the IDEs with smaller feature sizes demonstrated the most favorable sensing characteristics as they were more sensitive (change in diameter of semicircle, $\Delta R_{ct}$) to variations in the KCl concentration as impedance values recorded for IDEs with the smallest to largest feature sizes were 21, 17, and 4.5 kΩ. These results demonstrate that the IDE fabricated using the IML method displayed standard EIS characteristics and hence can act as a viable EIS sensor; furthermore, decreasing the feature size of the electrochemical sensors can improve sensor sensitivity.



DOI: 10.1021/acsnano.7b03554
*ACS Nano* 2017, 11, 9836–9845

## CONCLUSIONS

In summary, a micromanufacturing technique of depositing graphene films for high-resolution patterning has been demonstrated using a technique coined IML. This method can pattern solutions not easily inkjet printable such as inks comprising high nanoparticle concentrations, large particle sizes, or higher viscosities. This developed IML process creates smaller feature sizes than conventional inkjet printing as the feature size is not limited to the width of the jetted material but rather the space between two printed lines. In addition to high-resolution patterning, this process promotes rapid prototyping as no photolithography steps, stencils, or patterns are necessary.

Two different patterns were designed and tested to demonstrate the application of IML for electrochemical sensing. First, a $H_2O_2$ sensor was manufactured which showed the electroactive nature of the patterned and laser-annealed graphene electrodeposited platinum hybrid using the IML technique. The designed $H_2O_2$ sensor exhibited a low detection limit ($0.21 \pm 0.16$ $\mu$M), wide linear sensing range (0.1 to 550 $\mu$M), and fast response time (5 s)—the graphene films exhibited a high degree of electroactivity during electrochemical sensing. Next, IDEs of varying finger width and spacing (50 and 50 $\mu$m; 75 and 150 $\mu$m; 150 and 200 $\mu$m, respectively) were manufactured to demonstrate the ability to create distinct high-resolution graphene circuits rapidly *via* the IML process. The patterned graphene IDEs had sharp edges, consistent line width, and demonstrated characteristic EIS measurements such as a double layer capacitance of ~5 nF. EIS measurements revealed that the sensor sensitivity correlated to electrode feature size as the IDE with the smallest finger width and spacing (50 and 50 $\mu$m) displayed the largest EIS magnitude response in KCl (~21 KΩ). The developed IML technique can be used to pattern solution-phase graphene on diverse substrates such as silicon as well as flexible, disposable substrates including Kemafoil (heat treated PET), clear PET, and polyimide tape (Figure S8). We have also demonstrated that other inks such as those comprised of silver nanoparticles can be patterned with this IML technique (Figure S5). In summary, this work shows great promise in providing a rapid prototyping method of high-resolution patterns for concentrated, conductive nanoparticle inks which is compatible with multiple substrates. Hence, this technique could potentially have wide utility to applications that use patterned graphene including electrochemical sensors, energy harvesters, batteries, capacitors/supercapacitors, triboelectric nanogenerators, strain sensors, and chemical/biological sensors.[44,55−61]

## EXPERIMENTAL METHODS

**Materials.** Completely reduced graphene oxide (referred throughout as graphene) was purchased from ACS Materials (USA). All other chemicals including solvents were purchased from Sigma-Aldrich (USA) and used without any other further purification. The use of these chemicals is outlined in the following sections of this experimental procedure section.

**Polymer Lacquer Formulation and Printing.** Polymer lacquer ink was designed and optimized using an acrylic lacquer and diluted with solvents to an inkjet printable range. In short, 1 mL of a toluene formaldehyde nail polish was mixed with 1 mL of terpineol and 8 mL of cyclohexanone. The solution was then vortexed for 1 min and filtered using a 0.45 syringe filter. The viscosity and surface tension of the ink were measured using a Rheometer uVisc micropipette viscometer at 40 °C and were found to be 6 cP and 41 mN/m, respectively.

Inkjet printing of the polymer lacquer inks was conducted with a Fujifilm Dimatix Materials printer (DMP2800). The polymer sacrificial ink was loaded into a 3 mL printer cartridge and printed through 1 pL nominal drop volume nozzles. The waveform was adjusted to print nozzles at a temperature of 40 °C with a 20 $\mu$m drop spacing. These parameters yielded consistent droplets without any satellite droplets and well-defined lines that held tightly to the substrate. The ink was printed onto N-type ⟨1,0,0⟩ 300 nm dry thermal oxide polished silicon wafers (Silicon Quest International Inc.), polyimide (DuPont Kapton 125 $\mu$m), and heat-stabilized polyester film (Coveme, Kemafoil PET 100 $\mu$m). Typically, a single printed layer adequately forms the sacrificial layer, which dramatically increases the speed and resolution of IML over typical inkjet printing; however, porous materials required additional printing passes as the polymer was absorbed into the surface.

**Graphene Ink Formulation and Graphene Film Fabrication.** Graphene ink (10 mL) was synthesized by first vortexing 150 mg of completely reduced graphene oxide (ACS Material, GN1P0005, 1−5 $\mu$m flake size) in 50 mL of ethanol for 5 min at high speed in a 50 mL falcon vortex tube. Ethyl cellulose (viscosity 46 cP, 5% in toluene/ethanol 80:20(lit.), Sigma-Aldrich 433837) was added to the solution (25 mg/mL) and revortexed for 5 min on high to increase solution homogeneity. Next, 10 mL of terpineol (Sigma-Aldrich T3407) was added to the solution. The graphene ink was then poured into a 100 mL beaker and probe sonicated (Sonics Vibra-cell VCX-750 ultrasonic processor) at 70% amplitude with a 9 s pulse and 1 s rest for 2 h to break up large particles. The beaker was suspended in a bath sonicator, and the water was continually refreshed to provide cooling during sonication. The solution was then bath sonicated for 6 h at high power to break up the graphene into smaller particles. The bath temperature was refreshed to maintain a temperature of no more than 40 °C. The ethanol was then evaporated off by heating on a hot plate, leaving a concentrated graphene solution (15 mg/mL). This procedure provided a stable and homogeneous graphene ink with a viscosity well-suited for spin-coating (176.2 cP).

The graphene ink was spin-coated over the entire surface of the substrate including the inkjet printed sacrificial layer. One milliliter of graphene ink was pipetted on the center of the wafer and spin-coated at 1000 rpm for 30 s. The wafer was then heated at 90 °C on a hot plate for 2 min to dry the graphene ink. A postbake was performed in a convection furnace at 120 °C for 1 h to ensure the graphene thoroughly adhered to the substrate or baked with a heat gun for 10 min. The sacrificial layer was then removed in an acetone bath and impinged with acetone from a wash bottle or bath sonicated in a Branson 2800 series bath sonicator at low power for 10 s to remove excess graphene. It should be noted that adhesion between graphene flakes often created a thin graphene film layer that adhered to the edges of the patterned graphene and suspended over the sacrificial layer (Figure S9a). Hence, this thin graphene film layer impedes the graphene lift-off process and prevented straight edge graphene lines. To circumvent these deleterious effects, the graphene electrodes were sonicated in an acetone bath for 10 s at low power or impinged with acetone from a wash bottle to remove excess graphene (Figure S9b).

**Scanning Electron Microscopy.** The IML patterned graphene was investigated using a field emission scanning electron microscope (FEI Quanta 250). All images were captured using secondary electron mode, with a working distance of ~10 mm, spot size of 3.0, and with a 10 kV accelerating potential. A turbo pump sputter coater was used to deposit 2 nm of Iridium over the samples to ensure no surface charging or capacitance during SEM imaging.

**Atomic Force Microscopy.** AFM images of printed graphene layers on silicon wafer surfaces were acquired in PeakForce tapping mode using a Dimension Icon scanning probe microscope (Bruker, Santa Barbara, CA). The PeakForce tapping images were acquired using ScanAsyst. AFM probes used were model SCANASYST AIR (Bruker, Santa Barbara, CA). All images were acquired in air. AFM images were post-processed using plane-fitting (second-order) and/or flattening (zeroth-order) techniques with Nanoscope software.

**Confocal Microscopy.** Confocal microscopy (Sensofar, S-neox, Spain) measurements were performed to study the surface features of



DOI: 10.1021/acsnano.7b03554
ACS Nano 2017, 11, 9836−9845

printed graphene layers on prepared silicon wafers. An area of 350.88 × 264.19 $\mu m^2$ with 150× magnification was scanned with the SensoScan software. The *z*-scan was performed using a 0.1 $\mu$m step size. Form removal post-processing was performed to remove sample tilt.

**X-ray Photoelectron Spectroscopy.** XPS of IML patterned graphene before and after laser annealing was analyzed using a Kratos Amicus X-ray photoelectron spectrometer containing an Al K$\alpha$ excitation source (1486.7 eV). The binding energy scan was formed by subtracting the excitation energy from the measured photoelectron energy from the constituent elements. The C 1s spectrum fitted using CasaXPS with a Shirley background fitting and a Gaussian−Lorentzian line peak fitting on the constituent peaks.

**$H_2O_2$ Sensor Fabrication and Electrochemical Characterization.** All electrochemical measurements and procedures were conducted on a CH instrument potentiostat (600E series) in 1× PBS. The $H_2O_2$ sensors were fabricated using the IML method described herein. The electrodes were laser-annealed at laser power 1 and raster rate of 50 ms using a 1000 mW engraver with a blue-violet laser. Platinum was electrochemically deposited onto the graphene surface of the working electrode with a 2.5 mA/$cm^2$ current for 100 cycles following our similar established protocols for electrodepositing platinum nanoparticles on graphene and carbon nanotubes.[31,36,37,62] The $H_2O_2$ sensors were next placed in a 3D printed container to standardize testing between electrodes; these sensors were tested using a standard three-electrode setup with a Ag/AgCl single membrane reference electrode and a platinum wire counter electrode (Figure S10). Cyclic voltammograms were conducted with a scan rate 0.05 mV/s between the potential voltage of −0.2 to +0.6 V (Figure 5d). Amperometric voltammetry was conducted at +0.4 V as determined from cyclical voltammetry. Electrodes were polarized for approximately 250 s before $H_2O_2$ additions were added. $H_2O_2$ (Sigma-Aldrich H1009) dilutions in 1× PBS was then added to create final concentration additions of 0.1 $\mu$M through 100 $\mu$M. The response time of the sensor was defined as the time from initial $H_2O_2$ injection to the point at which 95% of the steady-state value was reached.

**Interdigitate Electrode Fabrication and Electrochemical Characterization.** Graphene IDEs were manufactured using the IML method on a silicon wafer as described throughout the article. The silicon wafer was then placed on a hot plate and thermally annealed at 300 °C in ambient air for 30 min. A carbon paste was deposited on the ends of the IDE for alligator clips to attach. The IDE was tested in a standard two-electrode setup by electrically shorting the reference and counter electrodes. Electrochemical impedance spectroscopy was conducted with 5 mV amplitude, frequency between 1 and $10^5$ Hz and no DC current bias. EIS was conducted in varying concentrations of KCl ($10^{-1}$, $10^{-2}$, $10^{-3}$, and $10^{-4}$ M). The double layer capacitance ($C_{dl}$) was calculated following the theory behind nonfaradaic EIS, which correlates $C_{dl}$ with phase ($\phi$) and impedance ($|Z|$) as a sampling function in the electrolyte solution. $C_{dl}$ is hence calculated from the Nyquist plot by taking the inverse of the product of the film resistance ($R_{ct}$, diameter of the semicircle) and angular frequency at top of the semicircle ($\omega_{maxZ''}$).

## ASSOCIATED CONTENT

### Supporting Information

The Supporting Information is available free of charge on the ACS Publications website at DOI: 10.1021/acsnano.7b03554.

Optical images of inkjet printed sacrificial layer, thermal and laser annealing temperature and time *versus* graphene resistance, XPS of unannealed and laser-annealed graphene, confocal microscopic images of IML graphene, graphene and silver patterning using IML, IDE design, SEM micrographs of graphene IDEs, graphene IML logos printed on various substrates, optical images of graphene suspended over a sacrificial layer, electrochemical sensing setup, and video captions (PDF)

Movie 1 (AVI)

Movie 2 (AVI)

## AUTHOR INFORMATION


### Corresponding Author

*E-mail: jcclauss@iastate.edu.

### ORCID

Jonathan C. Claussen: 0000-0001-7065-1077


### Notes

The authors declare no competing financial interest.

## ACKNOWLEDGMENTS

J.C.C. gratefully acknowledges funding support for this work by the National Institute of Food and Agriculture, U.S. Department of Agriculture, under Award Number 2016-67021-25038, the National Science Foundation under award number CBET-1706994, by the Roy J. Carver Charitable Trust Foundation under Award Number 15-4615, as well as by the Iowa State University College of Engineering and Department of Mechanical Engineering. Special thanks to D. Jing of the Materials Analysis Research Laboratory (MARL) of Iowa State University for assistance with XPS measurements.

## REFERENCES


(1) Nomura, K.-i.; Ushijima, H.; Nagase, K.; Ikedo, H.; Mitsui, R.; Sato, J.; Takahashi, S.; Nakajima, S.-i.; Arai, M.; Kurata, Y.; et al. Simultaneous Formation of Fine and Large-Area Electrode Patterns Using Screen-Offset Printing and Its Application to the Patterning on Adhesive Materials. *Jpn. J. Appl. Phys.* **2016**, *55*, 03DD01.

(2) Jiang, J.; Bao, B.; Li, M.; Sun, J.; Zhang, C.; Li, Y.; Li, F.; Yao, X.; Song, Y. Fabrication of Transparent Multilayer Circuits by Inkjet Printing. *Adv. Mater.* **2016**, *28*, 1420−1426.

(3) Bao, B.; Jiang, J.; Li, F.; Zhang, P.; Chen, S.; Yang, Q.; Wang, S.; Su, B.; Jiang, L.; Song, Y. Fabrication of Patterned Concave Microstructures by Inkjet Imprinting. *Adv. Funct. Mater.* **2015**, *25*, 3286−3294.

(4) Sokolov, A. N.; Roberts, M. E.; Bao, Z. Fabrication of Low-Cost Electronic Biosensors. *Mater. Today* **2009**, *12*, 12−20.

(5) Arias, A. C.; MacKenzie, J. D.; McCulloch, I.; Rivnay, J.; Salleo, A. Materials and Applications for Large Area Electronics: Solution-Based Approaches. *Chem. Rev.* **2010**, *110*, 3−24.

(6) Jang, J.; Ha, J.; Cho, J. Fabrication of Water-Dispersible Polyaniline-Poly (4-Styrenesulfonate) Nanoparticles for Inkjet-Printed Chemical-Sensor Applications. *Adv. Mater.* **2007**, *19*, 1772−1775.

(7) Le, L. T.; Ervin, M. H.; Qiu, H.; Fuchs, B. E.; Lee, W. Y. Graphene Supercapacitor Electrodes Fabricated by Inkjet Printing and Thermal Reduction of Graphene Oxide. *Electrochem. Commun.* **2011**, *13*, 355−358.

(8) Kovalchuk, A.; Huang, K.; Xiang, C.; Martí, A. A.; Tour, J. M. Luminescent Polymer Composite Films Containing Coal-Derived Graphene Quantum Dots. *ACS Appl. Mater. Interfaces* **2015**, *7*, 26063−26068.

(9) Zhang, S.; Li, S.; Cheng, S.; Ma, J.; Chang, H. Research on Smart Sensing Rfid Tags under Flexible Substrates in Printed Electronics. In *Electronic Packaging Technology (ICEPT), 2015 16th International Conference*; IEEE, 2015.

(10) Wilson, K. G.; Ovington, P.; Dean, D. A Low-Cost Inkjet-Printed Glucose Test Strip System for Resource-Poor Settings. *J. Diabetes Sci. Technol.* **2015**, *9*, 1275−1281.

(11) Geim, A. K. Graphene: Status and Prospects. *Science* **2009**, *324*, 1530−1534.

(12) Kostarelos, K.; Novoselov, K. S. Exploring the Interface of Graphene and Biology. *Science* **2014**, *344*, 261−263.

(13) Torrisi, F.; Hasan, T.; Wu, W.; Sun, Z.; Lombardo, A.; Kulmala, T. S.; Hsieh, G.-W.; Jung, S.; Bonaccorso, F.; Paul, P. J.; Chu, D.; Ferrari, A. C. Inkjet-Printed Graphene Electronics. *ACS Nano* **2012**, *6*, 2992−3006.




DOI: 10.1021/acsnano.7b03554
*ACS Nano* 2017, 11, 9836−9845

(14) He, Q.; Das, S. R.; Garland, N. T.; Jing, D.; Hondred, J. A.; Cargill, A. A.; Ding, S.; Karunakaran, C.; Claussen, J. C. Enabling Inkjet Printed Graphene for Ion Selective Electrodes with Postprint Thermal Annealing. *ACS Appl. Mater. Interfaces* **2017**, *9* (14), 12719−12727.
(15) Aleeva, Y.; Pignataro, B. Recent Advances in Upscalable Wet Methods and Ink Formulations for Printed Electronics. *J. Mater. Chem. C* **2014**, *2*, 6436−6453.
(16) Zhou, X.; Boey, F.; Huo, F.; Huang, L.; Zhang, H. Chemically Functionalized Surface Patterning. *Small* **2011**, *7*, 2273−2289.
(17) Secor, E. B.; Lim, S.; Zhang, H.; Frisbie, C. D.; Francis, L. F.; Hersam, M. C. Gravure Printing of Graphene for Large-Area Flexible Electronics. *Adv. Mater.* **2014**, *26*, 4533−4538.
(18) Hyun, W. J.; Secor, E. B.; Hersam, M. C.; Frisbie, C. D.; Francis, L. F. High-Resolution Patterning of Graphene by Screen Printing with a Silicon Stencil for Highly Flexible Printed Electronics. *Adv. Mater.* **2015**, *27*, 109−115.
(19) Weber, C. M.; Berglund, C. N.; Gabella, P. Mask Cost and Profitability in Photomask Manufacturing: An Empirical Analysis. *IEEE Trans. Semicond. Manuf.* **2006**, *19*, 465−474.
(20) Sanjana, N. E.; Fuller, S. B. A Fast Flexible Ink-Jet Printing Method for Patterning Dissociated Neurons in Culture. *J. Neurosci. Methods* **2004**, *136*, 151−163.
(21) Beidaghi, M.; Wang, C. Micro-Supercapacitors Based on Interdigital Electrodes of Reduced Graphene Oxide and Carbon Nanotube Composites with Ultrahigh Power Handling Performance. *Adv. Funct. Mater.* **2012**, *22*, 4501−4510.
(22) Singh, M.; Haverinen, H. M.; Dhagat, P.; Jabbour, G. E. Inkjet Printing—Process and Its Applications. *Adv. Mater.* **2010**, *22*, 673−685.
(23) Secor, E. B.; Prabhumirashi, P. L.; Puntambekar, K.; Geier, M. L.; Hersam, M. C. Inkjet Printing of High Conductivity, Flexible Graphene Patterns. *J. Phys. Chem. Lett.* **2013**, *4*, 1347−1351.
(24) Angelo, P. D. Inkjet-Printed Light-Emitting Devices: Applying Inkjet Microfabrication to Multilayer Electronics. Ph.D. Dissertation, University of Toronto, 2013.
(25) Lee, S. H.; Shin, K. Y.; Hwang, J. Y.; Kang, K. T.; Kang, H. S. Silver Inkjet Printing with Control of Surface Energy and Substrate Temperature. *J. Micromech. Microeng.* **2008**, *18*, 075014.
(26) Seng, L. C.; Chollet, F. Maskless Lithography Using Off-the-Shelf Inkjet Printer. In *Smart Materials, Nano- and Micro-Smart Systems*; International Society for Optics and Photonics, 2006.
(27) Nishimoto, S.; Kubo, A.; Nohara, K.; Zhang, X.; Taneichi, N.; Okui, T.; Liu, Z.; Nakata, K.; Sakai, H.; Murakami, T.; et al. Tio 2-Based Superhydrophobic−Superhydrophilic Patterns: Fabrication *Via* an Ink-Jet Technique and Application in Offset Printing. *Appl. Surf. Sci.* **2009**, *255*, 6221−6225.
(28) Sun, J.; Bao, B.; Jiang, J.; He, M.; Zhang, X.; Song, Y. Facile Fabrication of a Superhydrophilic−Superhydrophobic Patterned Surface by Inkjet Printing a Sacrificial Layer on a Superhydrophilic Surface. *RSC Adv.* **2016**, *6*, 31470−31475.
(29) Zhang, L.; Liu, H.; Zhao, Y.; Sun, X.; Wen, Y.; Guo, Y.; Gao, X.; Di, C. a.; Yu, G.; Liu, Y. Inkjet Printing High-Resolution, Large-Area Graphene Patterns by Coffee-Ring Lithography. *Adv. Mater.* **2012**, *24*, 436−440.
(30) Jahn, S. F.; Engisch, L.; Baumann, R. R.; Ebert, S.; Goedel, W. A. Polymer Microsieves Manufactured by Inkjet Technology. *Langmuir* **2009**, *25*, 606−610.
(31) Das, S. R.; Nian, Q.; Cargill, A. A.; Hondred, J. A.; Ding, S.; Saei, M.; Cheng, G. J.; Claussen, J. C. 3d Nanostructured Inkjet Printed Graphene *Via* Uv-Pulsed Laser Irradiation Enables Paper-Based Electronics and Electrochemical Devices. *Nanoscale* **2016**, *8*, 15870−15879.
(32) Das, S. R.; Uz, M.; Ding, S.; Lentner, M. T.; Hondred, J. A.; Cargill, A. A.; Sakaguchi, D. S.; Mallapragada, S.; Claussen, J. C. Electrical Differentiation of Mesenchymal Stem Cells into Schwann-Cell-Like Phenotypes Using Inkjet-Printed Graphene Circuits. *Adv. Healthcare Mater.* **2017**, *6*, 1601087.
(33) Secor, E. B.; Gao, T. Z.; Islam, A. E.; Rao, R.; Wallace, S. G.; Zhu, J.; Putz, K. W.; Maruyama, B.; Hersam, M. C. Enhanced Conductivity, Adhesion, and Environmental Stability of Printed Graphene Inks with Nitrocellulose. *Chem. Mater.* **2017**, *29*, 2332−2340.
(34) Derby, B.; Reis, N. Inkjet Printing of Highly Loaded Particulate Suspensions. *MRS Bull.* **2003**, *28*, 815−818.
(35) Siburian, R.; Sebayang, K.; Supeno, M.; Marpaung, H. Effect of N-Doped Graphene for Properties of Pt/N-Doped Graphene Catalyst. *ChemistrySelect* **2017**, *2*, 1188−1195.
(36) Claussen, J. C.; Kumar, A.; Jaroch, D. B.; Khawaja, M. H.; Hibbard, A. B.; Porterfield, D. M.; Fisher, T. S. Nanostructuring Platinum Nanoparticles on Multilayered Graphene Petal Nanosheets for Electrochemical Biosensing. *Adv. Funct. Mater.* **2012**, *22*, 3399−3405.
(37) Claussen, J. C.; Artiles, M. S.; McLamore, E. S.; Mohanty, S.; Shi, J.; Rickus, J. L.; Fisher, T. S.; Porterfield, D. M. Electrochemical Glutamate Biosensing with Nanocube and Nanosphere Augmented Single-Walled Carbon Nanotube Networks: A Comparative Study. *J. Mater. Chem.* **2011**, *21*, 11224−11231.
(38) Cargill, A. A.; Neil, K. M.; Hondred, J. A.; McLamore, E. S.; Claussen, J. C. Effect of Platinum Nanoparticle Deposition Parameters on Hydrogen Peroxide Transduction for Applications in Wearable Electrochemical Glucose Biosensors. In *SPIE Commercial+ Scientific Sensing and Imaging*; International Society for Optics and Photonics, 2016.
(39) Daniele, M. A.; Pedrero, M.; Burrs, S.; Chaturvedi, P.; Salim, W. W. A. W.; Kuralay, F.; Campuzano, S.; McLamore, E.; Cargill, A. A.; Ding, S. Hybrid Metallic Nanoparticles: Enhanced Bioanalysis and Biosensing *via* Carbon Nanotubes, Graphene, and Organic Conjugation. In *Nanobiosensors and Nanobioanalyses*; Springer, 2015; pp 137−166.
(40) Cui, X.; Wu, S.; Li, Y.; Wan, G. G. Sensing Hydrogen Peroxide Using a Glassy Carbon Electrode Modified with in-Situ Electrodeposited Platinum-Gold Bimetallic Nanoclusters on a Graphene Surface. *Microchim. Acta* **2015**, *182*, 265−272.
(41) Guo, S.; Wen, D.; Zhai, Y.; Dong, S.; Wang, E. Platinum Nanoparticle Ensemble-on-Graphene Hybrid Nanosheet: One-Pot, Rapid Synthesis, and Used as New Electrode Material for Electrochemical Sensing. *ACS Nano* **2010**, *4*, 3959−3968.
(42) Zhou, M.; Shang, L.; Li, B.; Huang, L.; Dong, S. Highly Ordered Mesoporous Carbons as Electrode Material for the Construction of Electrochemical Dehydrogenase-and Oxidase-Based Biosensors. *Biosens. Bioelectron.* **2008**, *24*, 442−447.
(43) Jia, N.; Huang, B.; Chen, L.; Tan, L.; Yao, S. A Simple Non-Enzymatic Hydrogen Peroxide Sensor Using Gold Nanoparticles-Graphene-Chitosan Modified Electrode. *Sens. Actuators, B* **2014**, *195*, 165−170.
(44) Bandodkar, A. J.; Jeerapan, I.; You, J.-M.; Nuñez-Flores, R.; Wang, J. Highly Stretchable Fully-Printed Cnt-Based Electrochemical Sensors and Biofuel Cells: Combining Intrinsic and Design-Induced Stretchability. *Nano Lett.* **2016**, *16*, 721−727.
(45) Kokkinos, C.; Economou, A.; Prodromidis, M. I. Electrochemical Immunosensors: Critical Survey of Different Architectures and Transduction Strategies. *TrAC, Trends Anal. Chem.* **2016**, *79*, 88−105.
(46) Min, J.; Baeumner, A. J. Characterization and Optimization of Interdigitated Ultramicroelectrode Arrays as Electrochemical Biosensor Transducers. *Electroanalysis* **2004**, *16*, 724−729.
(47) Teerapanich, P.; Myint, M. T. Z.; Joseph, C. M.; Hornyak, G. L.; Dutta, J. Development and Improvement of Carbon Nanotube-Based Ammonia Gas Sensors Using Ink-Jet Printed Interdigitated Electrodes. *IEEE Trans. Nanotechnol.* **2013**, *12*, 255−262.
(48) Marrakchi, M.; Jaffrezic Renault, N.; Dzyadevych, S.; Lagarde, F.; Samuelson, J. P. Pollutant Detection and Environemental Monitoring Using Conductometric Microbiosensors Industrial Waste. In *Industrial Waste. Environmental Impact, Disposal and Treatment*; Nova Publishers, 2009; pp 205−222.


DOI: 10.1021/acsnano.7b03554
*ACS Nano* 2017, 11, 9836−9845

(49) Laureyn, W.; Van Gerwen, P.; Suls, J.; Jacobs, P.; Maes, G. Characterization of Nanoscaled Interdigitated Palladium Electrodes of Various Dimensions in Kcl Solutions. *Electroanalysis* **2001**, *13*, 204−211.
(50) Ibrahim, M.; Claudel, J.; Kourtiche, D.; Nadi, M. Geometric Parameters Optimization of Planar Interdigitated Electrodes for Bioimpedance Spectroscopy. *J. Diabetes Sci. Technol.* **2013**, *4*, 13−22.
(51) Van Gerwen, P.; Laureyn, W.; Laureys, W.; Huyberechts, G.; De Beeck, M. O.; Baert, K.; Suls, J.; Sansen, W.; Jacobs, P.; Hermans, L.; et al. Nanoscaled Interdigitated Electrode Arrays for Biochemical Sensors. *Sens. Actuators, B* **1998**, *49*, 73−80.
(52) Dharuman, V.; Grunwald, T.; Nebling, E.; Albers, J.; Blohm, L.; Hintsche, R. Label-Free Impedance Detection of Oligonucleotide Hybridisation on Interdigitated Ultramicroelectrodes Using Electrochemical Redox Probes. *Biosens. Bioelectron.* **2005**, *21*, 645−654.
(53) Zou, Z.; Kai, J.; Rust, M. J.; Han, J.; Ahn, C. H. Functionalized Nano Interdigitated Electrodes Arrays on Polymer with Integrated Microfluidics for Direct Bio-Affinity Sensing Using Impedimetric Measurement. *Sens. Actuators, A* **2007**, *136*, 518−526.
(54) Yang, L.; Guiseppi-Wilson, A.; Guiseppi-Elie, A. Design Considerations in the Use of Interdigitated Microsensor Electrode Arrays (Imes) for Impedimetric Characterization of Biomimetic Hydrogels. *Biomed. Microdevices* **2011**, *13*, 279−289.
(55) Bandodkar, A. J.; Mohan, V.; López, C. S.; Ramírez, J.; Wang, J. Self-Healing Inks for Autonomous Repair of Printable Electrochemical Devices. *Adv. Electron. Mater.* **2015**, *1*, 1500289.
(56) El-Kady, M. F.; Strong, V.; Dubin, S.; Kaner, R. B. Laser Scribing of High-Performance and Flexible Graphene-Based Electrochemical Capacitors. *Science* **2012**, *335*, 1326−1330.
(57) Cong, H.-P.; Ren, X.-C.; Wang, P.; Yu, S.-H. Flexible Graphene−Polyaniline Composite Paper for High-Performance Supercapacitor. *Energy Environ. Sci.* **2013**, *6*, 1185−1191.
(58) Kim, B. J.; Jang, H.; Lee, S.-K.; Hong, B. H.; Ahn, J.-H.; Cho, J. H. High-Performance Flexible Graphene Field Effect Transistors with Ion Gel Gate Dielectrics. *Nano Lett.* **2010**, *10*, 3464−3466.
(59) Kim, S.; Gupta, M. K.; Lee, K. Y.; Sohn, A.; Kim, T. Y.; Shin, K. S.; Kim, D.; Kim, S. K.; Lee, K. H.; Shin, H. J.; et al. Transparent Flexible Graphene Triboelectric Nanogenerators. *Adv. Mater.* **2014**, *26*, 3918−3925.
(60) Tian, H.; Shu, Y.; Cui, Y.-L.; Mi, W.-T.; Yang, Y.; Xie, D.; Ren, T.-L. Scalable Fabrication of High-Performance and Flexible Graphene Strain Sensors. *Nanoscale* **2014**, *6*, 699−705.
(61) Liu, X.; Zhang, J.; Si, W.; Xi, L.; Eichler, B.; Yan, C.; Schmidt, O. G. Sandwich Nanoarchitecture of Si/Reduced Graphene Oxide Bilayer Nanomembranes for Li-Ion Batteries with Long Cycle Life. *ACS Nano* **2015**, *9*, 1198−1205.
(62) Claussen, J. C.; Hengenius, J. B.; Wickner, M. M.; Fisher, T. S.; Umulis, D. M.; Porterfield, D. M. Effects of Carbon Nanotube-Tethered Nanosphere Density on Amperometric Biosensing: Simulation and Experiment. *J. Phys. Chem. C* **2011**, *115*, 20896−20904.



DOI: 10.1021/acsnano.7b03554
*ACS Nano* 2017, 11, 9836−9845